Open circuit voltage profiling as diagnostic tool during stack lifetime testing

J. Stumper*, R. Rahmani, F. Fuss

Automotive Fuel Cell Cooperation, 9000 Glenlyon Parkway, Burnaby, BC, V5J 5J8, Canada

ARTICLE INFO

ABSTRACT

A 10-cell Mk 9 stack was characterized using current/voltage mapping during automotive drive cycle testing. A minimally invasive current mapping technique was used to determine localized polarization curves which together with open circuit voltage (OCV) profile measurements provide useful information about crossover leak formation and location. Through a systematic variation of reactant gas pressures it is further possible to distinguish between electrical shorts, diffusive and convective leaks.

© 2010 Published by Elsevier B.V.

1. Introduction

Advanced diagnostic methods that provide deeper insights into the relationship between cell design, operating conditions and cell performance and degradation are essential in order to meet the cost, durability, power density and freeze-startup targets necessary for PEM fuel cell commercialization. Consequently, AFCC and Ballard have been developing diagnostic test methods related to water management, localized performance measurement as well as the cell voltage loss breakdown (VLB) into kinetic, ohmic and mass transport related components [1,2]. Recently, these methods have been integrated into a fast dynamic test station capable of simulating automotive drive cycles enabling the measurement of current and voltage distributions in real time during dynamically changing operating conditions. By combining current mapping with specific diagnostic protocols, such as for example current–voltage sweeps under air/O_2 operation, local polarizations can be obtained within each cell of a stack. Through a fit of the Srinivasan equation [3] to these local polarizations, the spatially resolved VLB can be determined for each cell. Furthermore, the evolution of the VLB over time together with the change in active Pt-surface area (EPSA) can be used to generate so-called in situ degradation "fingerprints" [4] that are characteristic of a given degradation mode.

This paper illustrates how spatially resolved open circuit voltage (OCV) profiles and current–voltage sweeps can be used to monitor leak formation and growth with spatial resolution and

how to determine the type of leak (reactant crossover, electrical short) using a systematic variation of operating pressure. This approach provides valuable failure mode diagnostics and can be used to improve understanding of membrane degradation phenomena during stack lifetime testing.

2. Experimental

A Ballard Mk 9 10-cell stack was equipped with a current mapping setup which consisted of (i) segmented (16-fold) bus plates at both the anode and cathode end and (ii) cell voltage monitoring at eight locations along the cell length, positioned along one of the long sides of the cells (see Fig. 1). This arrangement provided spatial resolution of cell- and in-plane voltages along the fluid flow direction and also enabled the use of standard Membrane Electrode Assemblies (MEA's) and flowfield plates without any modifications (minimally invasive current mapping). The stack was subjected to an automotive drive cycle test that consisted of four 2 h dynamic operation blocks followed by 15 min shutdowns. Operating conditions during drive cycle testing were variable, ranging as follows: RH: 75–90%; inlet temperature: 60 °C; reactant pressures: 15–22 psig; load: 0–1.5 A cm^{-2}; oxidant gas: air; fuel gas: 80–100% H_2 balanced with N_2. The anode and cathode shunts were used to calculate the in(out)going current distribution, the through plane current distribution within each cell can then be calculated using a simple electrical network model once the in-plane resistances R_{jk}^{IP} of the bipolar plates are known. For this, cell voltage measurements at the positions corresponding to the bus plate segments were determined by interpolation using the eight measured values for each cell. EPSA measurements were performed using CO-stripping

* Corresponding author. Tel.: +1 604 412 3169; fax: +1 604 415 7291.
E-mail address: jurgen.stumper@afcc-auto.com (J. Stumper).
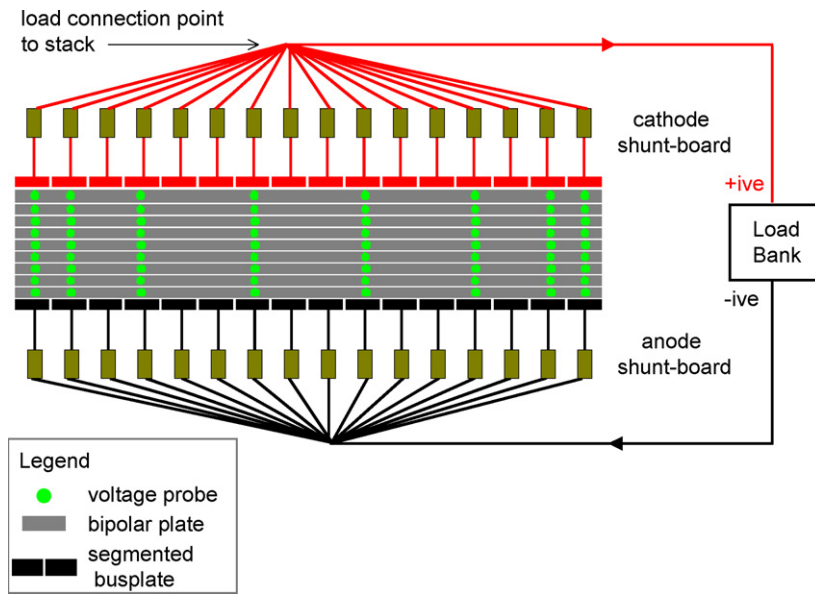
Fig. 1. Schematic diagram of the current mapping setup for the 10-cell Mk 9 stack. Both anode and cathode bus plates are divided into 16 segments or "pucks". In combination with the cell-voltage probing along the cell length this allows current mapping across all cells in a minimally invasive manner.

voltammetry by applying a voltage ramp to the whole stack using a programmable power supply.

In order to determine R_{jk}^{IP}, a special calibration procedure was developed. Ten special "calibration" MEA's were prepared where the membrane was removed selectively only in the areas of segment 1 or 16 in order to create electrical shorts. A stack was prepared with 10 calibration MEA's with shorts alternating in segments 1 and 16 and connected to a power supply to force a current in a zig-zag pattern through each of the bipolar plates. The stack temperature was kept at 60 °C and current–voltage characteristics were obtained by varying the power supply voltage. The observed current–voltage characteristics were linear allowing for the experimental determination of all 176 R_{jk}^{IP} under operating conditions representative of drive cycle operation.

3. Results and discussion

A 10-cell stack was subjected to a dynamic automotive drive cycle and performance diagnostics was performed at various points during duration of the test. The performance diagnostics consisted of cell voltage (I-V polarization) scan, EPSA determination and OCV measurement. Fig. 2 shows the evolution of the average cell voltages at 1.2 A cm^{-2} for each cell during the test. Based on the cell performance in Fig. 2a three distinct phases can be distinguished

1. Run-in or conditioning phase (<15% test duration)
2. Performance phase with only minimal and constant degradation (15% up to 80% test duration)
3. Final degradation phase characterized significantly increased degradation rates and large cell-to-cell voltage variations (80% to 100% test duration)

Fig. 2b shows that the stack voltage degradation in the performance phase is dominated by cells 9 and 10. The phenomenon that end-cells show much higher degradation rates and therefore dominate stack voltage degradation has been observed before and has been attributed to (i) different cell temperatures, (ii) reactant flow mal-distribution or (iii) a combination of the two. It is interesting to note that the high degrading cells are located at the cathode end of the stack, which suggests that liquid water accumulation on

the cathode side may be a contributing factor. Fig. 2c shows that the active Pt- surface area on the cathode decays for all cells, with cell 9 exhibiting the greatest degradation ($\approx$40% EPSA loss after 50% test duration). Consequently, catalyst degradation could be an additional cause for the observed high degradation for this cell.
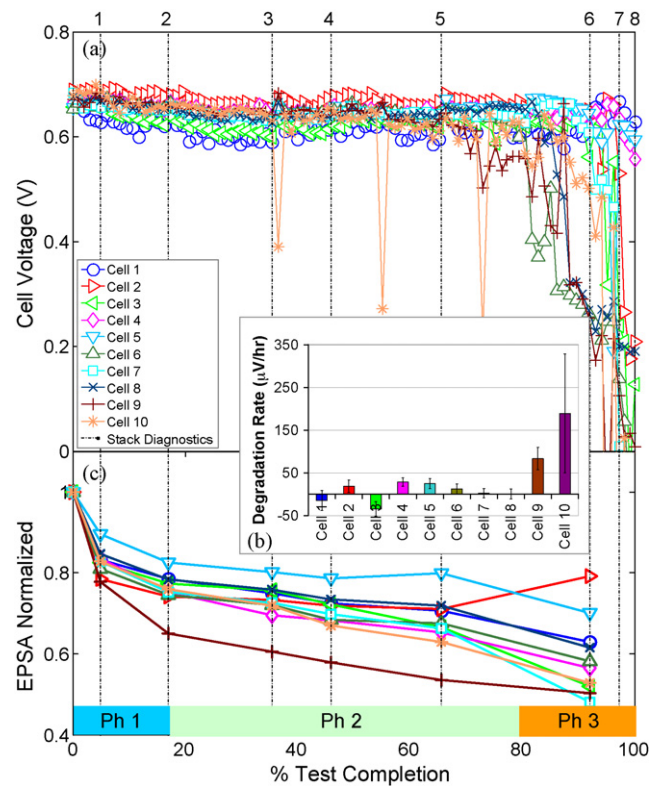
Fig. 2. (a) Lifetime plot of average cell voltage at 1.1 A cm^{-2} for a 10-cell Mk 9 stack during automotive drive cycle testing, vertical dash-dotted lines indicate times of performance diagnostics #1–8. The three performance phases Ph 1–3 are also indicated (see text). Error bars indicate 95% confidence intervals. (b) Average cell voltage degradation rates (negative values indicate performance increase) for cells 1–10 during performance phase (15% up to 80% test duration). (c) Normalized average EPSA loss for cells 1–10 during test duration.

Negative degradation rates (cells 1 and 3) are found in some cells of a stack from time to time even without apparent special cause, consequently this observation can be interpreted as due to natural statistical variation.

An exponential loss of EPSA has been reported before, for example during voltage cycling in H_2/N_2 atmosphere [5] and was attributed to an increase in Pt particle size [6].

Voltage loss breakdown analysis using a fit of the Srinivasan equation (see Eq. (4)) to the current voltage characteristics provides further insights into the nature of the performance degradation during the three phases of the test which can be summarized as follows [4]:

1. Run-in phase

    The initial performance drop in this phase is mostly due to an increase in kinetic loss accounting for $\geq$75% of the total loss, with the remainder due to mass transport effects. This is consistent with the rapid initial decrease in EPSA in Fig. 2c, amounting to about $\geq$50% of the total EPSA loss during the whole test. In this phase we also observe an increase in OCV (see Fig. 3) for all cells, which correlates with a decrease in the total leakage current j^L (see Fig. 8a), possibly caused by a reduction in H_2 crossover due to Pt- migration into the membrane.

2. Performance Phase

    In this phase the stack performance at first deteriorates further but then improves so that the overall performance degradation in this phase is almost zero, except for cells 9 and 10. For cells 1–8 kinetic and mass transport losses follow the same pattern whereas the ohmic loss is unchanged for all cells. For cells 9 and 10 the high degradation in this phase is caused by an increase in ohmic and mass transport losses.
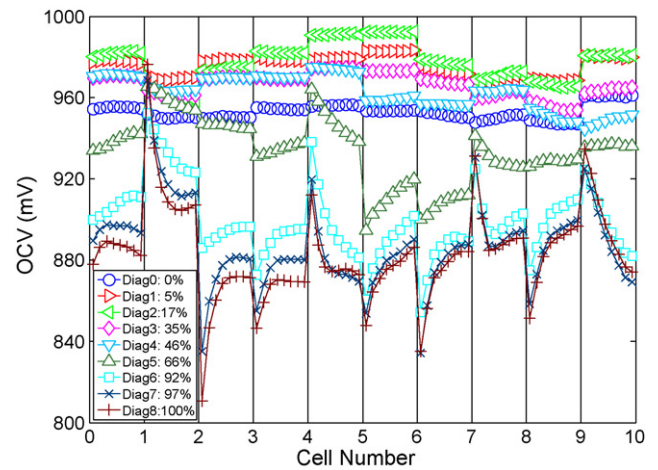
3. Final degradation phase

    This phase is characterized by a significant increase in kinetic and mass transport losses, and for cells 9, 10 also in ohmic loss. As seen in Fig. 3, this phase also shows a drastic drop in open circuit voltages, indicating membrane failure.

Fig. 4 shows that as the open circuit voltages decreases during the test, the OCV profiles along the cell become more and more variable. Towards the end of the test distinct OCV minima are observed in cells 3, 4, 6, 7 and 9 which are located consistently at the cell inlets, indicating that crossover leaks and/or electrical shorts are located there. The observed overall variation in OCV along the cell
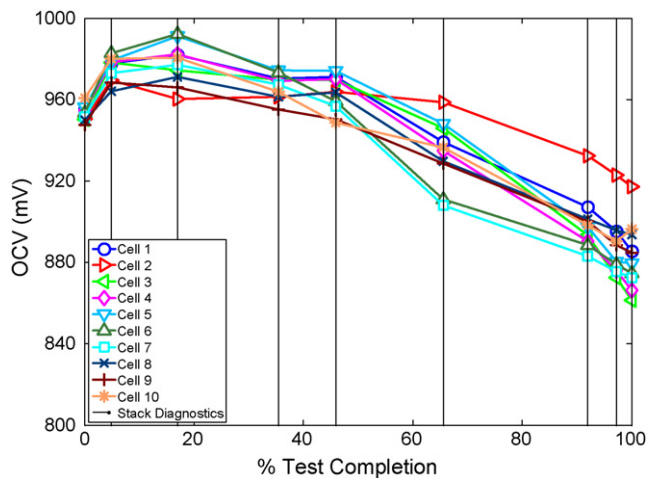
Fig. 4. Evolution of open circuit voltage profiles along the cell length for each cell of a 10-cell stack during lifetime testing, the legend indicates the times for diagnostics # 0–8 (see also Fig. 2). Operating conditions: $T = 60\,°C$, H_2/air pressure: 1.92/1.92 barg; anode/cathode flow rates: 30/100 slpm; anode/cathode RH: 100/100%; spatial resolution is 16/cell.

reaches up to 60 mV (cells 3 and 9). Furthermore, cells 6 and 7 show the earliest onset in OCV degradation.

In the next section, an electrical network model for the stack will be presented and used to better understand this type of data and extract more detailed information about leak type and location.

3.1. Electrical network model

Fig. 5 shows the network model to be used for a more detailed understanding of the OCV profiles shown in Fig. 4. The inset shows the mesh formed by the k-th and $(k+1)$-th segment of the j-th cell of the stack. The fuel cell of each segment is represented by a voltage source E_{jk}^0 in series with a nonlinear resistor R_{jk}. Leakage in each fuel cell segment is represented by a resistor R_{jk}^L, in parallel to the series combination of E_{jk}^0, R_{jk}.

The cell voltage for each segment can be written as:

$$E_{jk} = E_{jk}^0 - I_{jk}^s R_{jk} \tag{1}$$

where

$$R_{jk} = R_{jk}^\Omega + \frac{b_{jk}}{I_{jk}^s} \log\left(\frac{I_{jk}^s}{I_{jk}^0}\right) \tag{2}$$

and R_{jk}^Ω, b_{jk}, I_{jk}^0, denote the ohmic resistance, Tafel slope and exchange current for segment jk, respectively; the other current symbols are given in Fig. 5. It follows that:
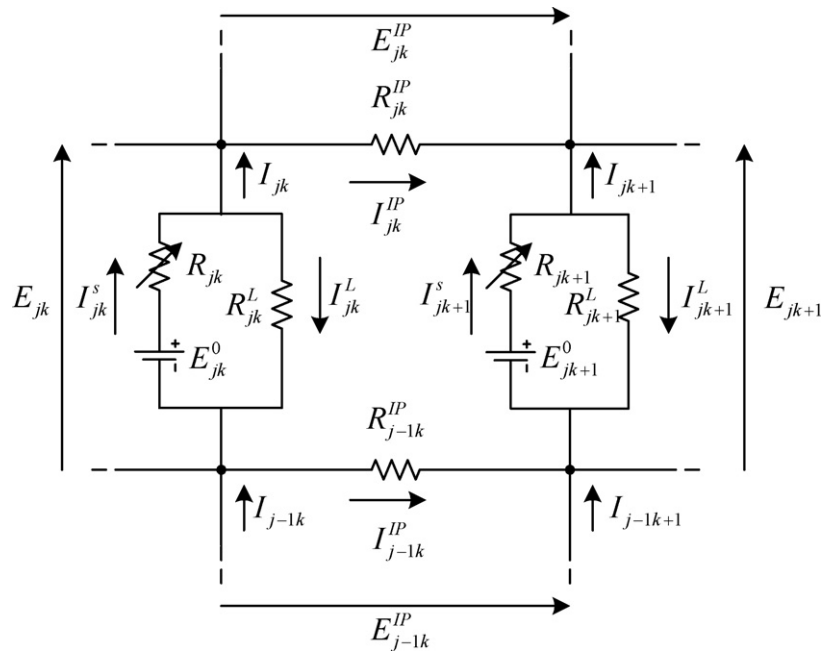
$$I_{jk}^s = I_{jk} + I_{jk}^L \tag{3}$$

and Eq. (1) can be written as

$$E_{jk} = E_{jk}^0 - b_{jk}\log\left(\frac{I_{jk} + I_{jk}^L}{I_{jk}^0}\right) - (I_{jk} + I_{jk}^L)R_{jk}^\Omega \tag{4}$$

Because $I_{jk}^L R_{jk}^\Omega$ is constant during a polarization scan and in the order of 10 mV ($I_{jk}^L \leq 0.1\,A\,cm^{-2}$ and $R_{jk}^\Omega \approx 0.1\,\Omega\,cm^2$), Eq. (4) can be simplified to:

$$E_{jk} = E_{jk}'^0 - b_{jk}\log\left(\frac{I_{jk} + I_{jk}^L}{I_{jk}^0}\right) - I_{jk}R_{jk}^\Omega \tag{5}$$

Fig. 3. Lifetime plot of the cell averaged OCV's for the individual cells of a 10-cell Mk 9 stack during automotive drive cycle testing, vertical dash-dotted lines indicate times of performance diagnostics. Cells 2/6,7 show the lowest/largest decrease in OCV.

Fig. 5. Elementary cell of the electrical network model for the 10-cell stack consisting of segments k, $k+1$ of the j-th cell showing the nomenclature of the individual currents, resistances and voltages. E_{jk}, E_{jk+1}, I_{j-1k}^{IP}, I_{jk}^{IP} are measured directly, whereas R_{jk}, R_{jk+1}, E_{jk}^0, E_{jk+1}^0, I_{jk}^L, I_{jk+1}^L are determined from a fit of Eq. (5) to the localized polarization curves.

where $E_{jk}'^0 = E_{jk}^0 - I_{jk}^L \cdot R_{jk}^\Omega \cong E_{jk}^0$. For simplicity we now assume

for all $j \in 1, \ldots, 10$ $\quad \sum_k I_{jk} = 0$ $\qquad$ (6)

i.e. no cell-internal electrical shorts, consequently internal gas leaks can only cause loop currents inside each cell. Using the network model the local through plane currents I_{jk} in each cell can now be calculated by proceeding successively from cell-to-cell starting from either end of the stack. E_{jk}, E_{jk+1}, are measured directly, I_{j-1k}^{IP}, I_{jk}^{IP} are calculated using the known in-plane resistances R_{jk}^{IP}, and R_{jk}^Ω, R_{jk+1}^Ω, E_{jk}^0, E_{jk+1}^0, I_{jk}^0, I_{jk+1}^0, I_{jk}^L, I_{jk+1}^L are determined from a fit of Eq. (5) to the localized polarization curves E_{jk}, (I_{jk}) measured at the same time as the OCV profiles.

3.2. Analysis of OCV profiles over lifetime

Fig. 6 shows the result of a calculation illustrating the effect of a reactant gas crossover leak in the middle of a cell within a 5-cell stack on the OCV profiles. Displayed are resulting through plane currents I_{jk}, as well as the in-plane currents I_{jk}^{IP}. If H_2 crosses over from A → C due to a leak in the membrane, the local cathode potential decreases due to mixed potential effects as the H_2 is oxidized either chemically or electrochemically. The result is an increase in local H^+-concentration at the cathode, leading to back-diffusion towards the anode as indicated by the downwards-pointing (red) arrow in the middle of cell 3. This reversal of the current is a consequence of the fact that more H_2 is oxidized at the cathode than at the anode [7]. This current is compensated by the sum of the upwards-pointing (blue) arrows in cell 3 so that Eq. (6) is fulfilled for all cells. Fig. 6 serves to illustrate the effect of a localized leak in a semi-quantitative manner: in the ideal case with no localized leaks or electrical shorts all currents I_{jk} are zero at OCV (although not necessarily the I_{jk}^L, as the H_2 crossover could be homogeneous along the length of the cell, in which case all I_{jk}^L are equal). However, any spatial variation in H_2 leakage to the cathode will lead to a reverse current I_{jk} (downward (red) arrow) at the location with the largest leak because of the reduction in

local OCV. Because we assume no electrical shorts no net electronic current is flowing and the sum of all I_{jk} still has to add up to zero. This is the cause for the different current direction along the cell.

The figure also shows the reduction in local OCV at the location of the leak, leading to a potential gradient along the bipolar plates, which in turn leads to in-plane currents as indicated by the horizontal arrows. Due to the potential gradients along the plates the neighboring cells are also affected, exhibiting current reversal in a similar fashion but with decreasing intensity the larger the distance from the leak. An internal transfer leak therefore has a characteristic signature, which in this graphical representation consists of a
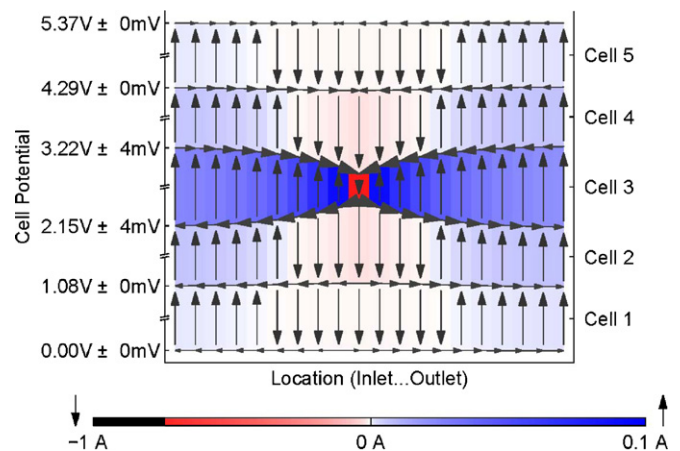
Fig. 6. OCV profiles and internal currents I_{jk} calculated theoretically for a 5-cell stack with a reactant gas crossover leak in the middle of cell 3 (electrical shorts excluded) corresponding to a leakage current of $I_{3,10}^L = 1$ A. Through plane currents: colour intensity codes magnitude [A], blue: current in same direction as during normal operation (H^+ movement from A → C), red: H^+ movement from C → A (current reversal). Y-axis labels indicate the cell voltages E_{jk} measured against the anode bus plate and are represented as $E \pm \Delta E$: where $E = (E_{jk\,max} + E_{jk\,min})/2$, $\Delta E = (E_{jk\,max} - E_{jk\,min})/2$ and $E_{jk\,max}$, $E_{jk\,min}$ refer to the maximum, minimum values for cell j, respectively. (For interpretation of the references to colour in this figure legend, the reader is referred to the web version of this article.)

localized down arrow in the apex of a fading double cone of down arrows.

It can be shown that the strength of the cell-to-cell coupling is determined by the bipolar plate resistivity (or the R_{jk}^{IP}). The lower the plate resistivity, the stronger and more localized is the effect on neighboring cells, i.e. the smaller the angle of the cone. A similar behaviour has been reported before, albeit for a different type of perturbation/anomaly (bus plate material change, partially inactive cell located at the stack center) in a stack [8]. Fig. 6 shows that current reversal in cell #3 is due to H_2 crossover, whereas current reversal in the neighboring cells is caused by the increase in local OCV as the sum of the cell voltages is constant at each position along the stack length (assuming equipotential bus plates). In order to support this reversed current, the neighboring cells are driven into local electrolysis mode. This could lead/contribute to localized catalyst degradation, particularly on the cathode. This also explains the pattern observed in Fig. 4, where the low OCV's at the inlets of cells 3, 4, 6, 7 and 9 are compensated by high voltages in cells, 2, 5, 8 and 10. Consequently, Fig. 6 suggests that the spatially resolved measurement of OCV profiles in combination with the local through plane current distribution enables the determination of leak location and magnitude in a minimally invasive fashion and that the monitoring of these characteristics over time can provide valuable data on membrane degradation.

Fig. 7 shows the OCV "current maps" I_{jk}, I_{jk}^{IP} calculated using the spatially resolved OCV data shown in Fig. 4. In order to solve for the unknowns I_{jk}, I_{jk}^{L}, the parameters b_{jk}, I_{jk}^{0} were determined

from a polarization scan taken at the same time as the OCV profiles. Together with the experimental voltages E_{jk}, E_{jk}^{IP}, this allowed the determination of the through plane, leakage and in-plane currents. The figure shows only the last four diagnostic OCV current maps #5–8 as only these correspond to significant changes compared to BOL. It can be seen that already at about 66% test duration leaks are starting to form at the cell inlets, in particular at cells 6 and 7. Comparison with Fig. 2a suggests that this might correlate with the performance decay observed after the weak performance maximum between diagnostics # 4 and # 5. The fact that this occurs well in the performance phase where the high load performance is largely unaffected, demonstrates the sensitivity of OCV profiling towards internal leak formation. Subsequently, strong leaks are also developing at the inlets of cells # 3 and 4 as well as somewhat weaker ones around segment #4 in cells # 2 and 9. The current reversals at segment #4 in cell 8 as wells segment #1 in cells 5, 8 and 10 are probably due to neighbor interactions (see Fig. 6), because they are associated with high cell voltages.

An alternative method to determine the leak rate is through a fit of Eq. (4) to the polarization scans; Fig. 8 a and b shows the integral leak rates $I_j^L = \sum_k I_{jk}^L$ calculated in this fashion together with the leak distribution at the end of the test, respectively. The leak rate first shows an initial decrease until about 30% test completion and thereafter an exponential increase indicating membrane failure. A similar exponential rise has been observed during OCV durability testing [9] as well as during operation under sub-saturated conditions [10].
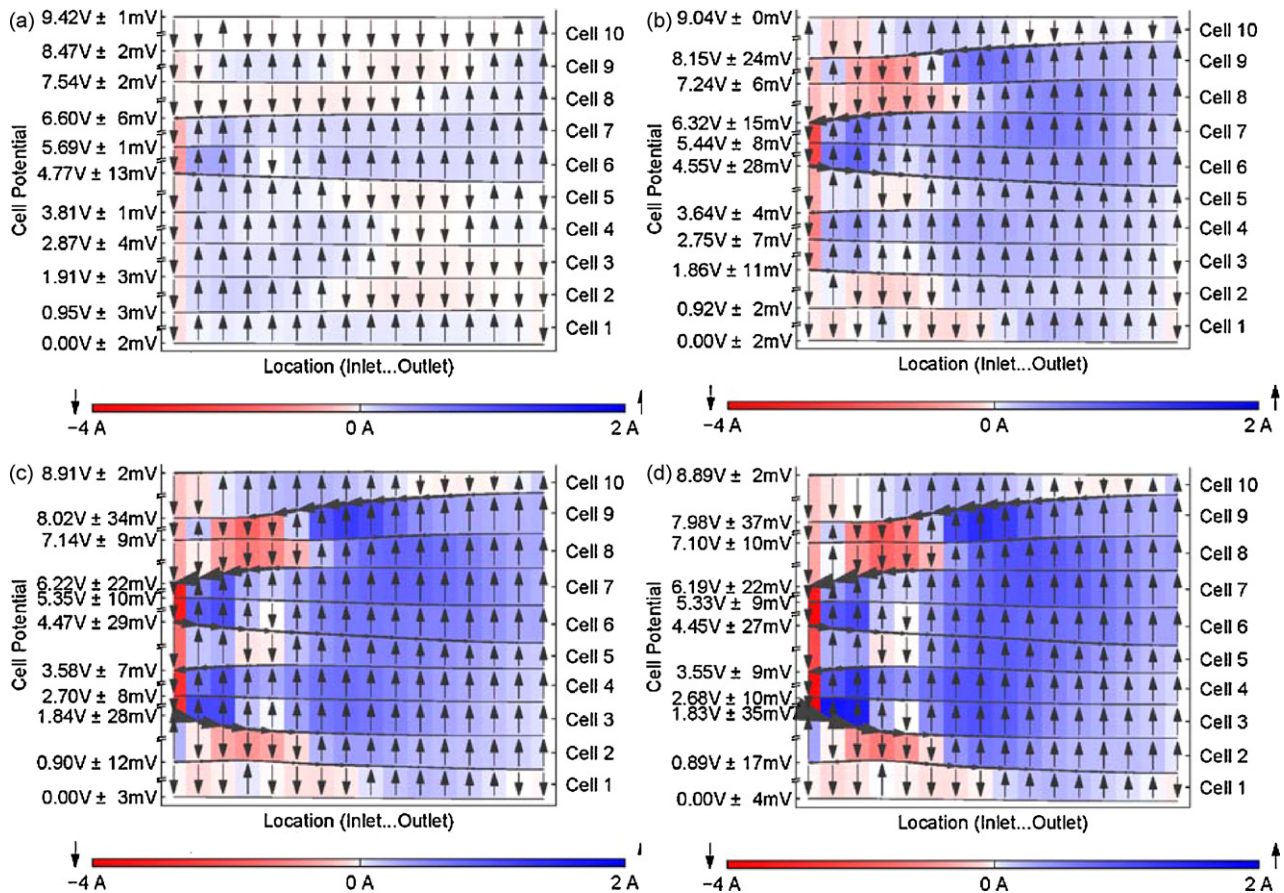

Fig. 7. (a)–(d): Measured OCV profiles and the corresponding calculated through plane currents I_{jk} at 66, 92, 97 and 100% test completion, respectively (see also Fig. 4). For the calculations, electrical shorts were excluded, i.e. Eq. (6) was assumed to hold. In-plane currents: arrow weight proportional to current in Amps. Y-axis labels indicate the cell voltages E_{jk} measured against the anode bus plate and are represented as $E \pm \Delta E$: where $E = (E_{jk\,max} + E_{jk\,min})/2$, $\Delta E = (E_{jk\,max} - E_{jk\,min})/2$ and $E_{jk\,max}$, $E_{jk\,min}$ refer to the maximum, minimum values for cell j, respectively.
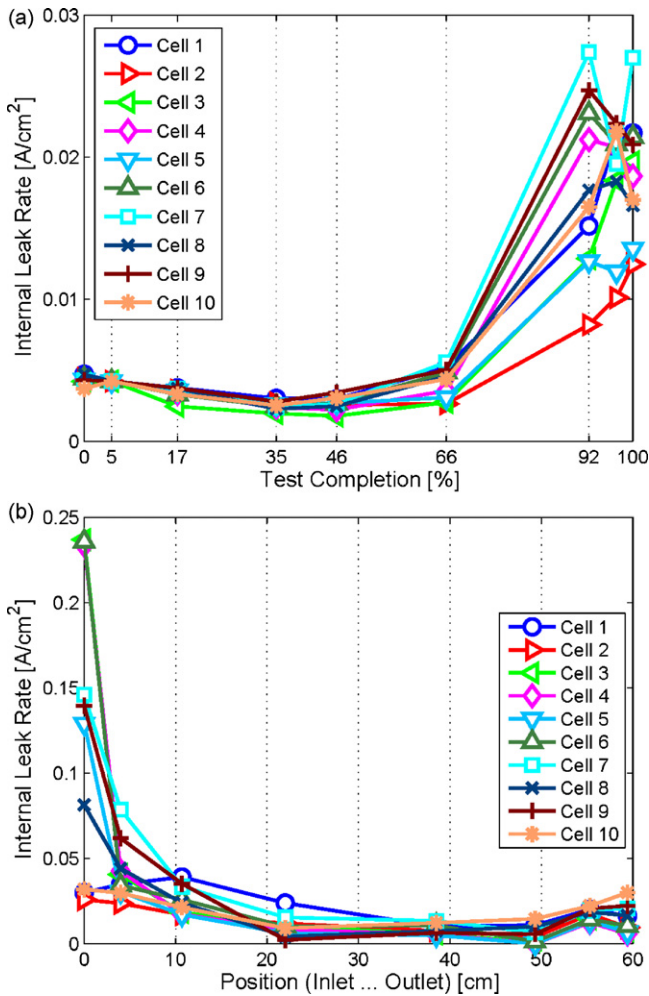
Fig. 8. Leakage currents calculated from a fit to the spatially resolved stack polarization curves (a) Total internal leak rates $I_j^L = \sum_k I_{jk}^L$ over time. From beginning of life (BOL) to middle of life (MOL) there is a slight decrease in internal leaks. Cells 6 and 7 are the first to develop internal leaks. Approaching EOL (100% test completion) most cells exhibit major leaks. (b) Spatially resolved leakage currents I_{jk}^L at EOL indicating leak formation predominantly at the inlets.

In summary there is good agreement between the leak rates determined from polarization fitting and the OCV profiles during lifetime performance testing. Both methods detect the same key features: leak formation commences at about 60% test duration and the leaky cells 3,4, 6,7 also show highest inlet rates in Fig. 8b. However, the OCV results are fairly sensitive to any reactant pressure differential Δp between anode and cathode and therefore care needs to be taken to keep $\Delta p \approx 0$ during the measurements.

3.3. Determination of leak type

Whereas the previous discussion focused on the determination of size and location of reactant transfer leaks, the leak type could not be determined; for example it was not possible to distinguish between a reactant transfer leak and an electrical short because both phenomena lead to current leakage. In general, the following physical processes can manifest themselves as an equivalent leakage current I_L:

- Reactant gas diffusion, driven by partial pressure gradients
- Reactant gas crossover flow, driven by pressure differentials (convective flow)
- Electrical shorts

We therefore can postulate the following dependency of I_L on the reactant gas partial pressures p_{O_2}, p_{H_2} and total pressures on the anode and cathode p_A^{tot}, p_C^{tot}:

$$\frac{I^L}{A} = j^L = j_0^L + L_H p_{H_2} + L_O p_{O_2} + L_x(p_A^{tot} - p_C^{tot}) \tag{7}$$

where

$$L_H = \frac{2 \cdot F \cdot D_{H_2}}{\Re \cdot T \cdot \delta_{mem}} \tag{8}$$

$$L_O = \frac{4 \cdot F \cdot D_{O_2}}{\Re \cdot T \cdot \delta_{mem}} \tag{9}$$

and $\Re$, F denote gas constant, Faraday's constant, T is the temperature, D is the diffusion coefficient and δ_{mem} is the membrane thickness. Because of its pressure independence, we can associate the term j_0^L with electrical shorts, whereas the coefficients L_H, L_O describe reactant gas diffusion and L_x convective reactant gas crossover flow, for example through pinholes.

Eq. (7) suggests that by using a systematic variation of operating variables such as reactant gas pressure and pressure differential between A, C, a further deconvolution of the total leakage current I_L into convective, diffusive and electrical short components is possible. In order to demonstrate the feasibility of this approach, a small test cell ($A = 50$ cm^2) was assembled using a MEA with a 25 μm Gore membrane and characterized with polarization scans at the conditions indicated in Fig. 9. Keeping p_{O_2} constant and using $p_{H_2} = p_A^{tot}$, Eq. (7) simplifies to:

$$j^L = (j_0^L + L_O p_{O_2}) + L_H p_{H_2} + L_x(p_{H_2} - p_C^{tot}) \tag{10}$$

By measuring j^L as function p_{H_2} and $\Delta p = p_{H_2} - p_C^{tot}$, L_x, L_H and the first term $j_0'^L = j_0^L + L_O p_{O_2}$ in Eq. (10) can be determined. Fig. 9 shows the results as a 2-D plot and it can be seen that for this cell the total leakage current j^L is dominated by a convective transfer leak. The test grid contained $5 \times 7 = 35$ points, and the three unknowns were determined (least squares solution) using the Moore–Penrose pseudo-inverse method [11] (see Table 1).

The value for the diffusive flow permeation coefficient is in the same order of magnitude as the H$_2$ permeation coefficient $\Psi_{H_2,L} \approx 4 \times 10^{-11}$ mol s^{-1} cm^{-1} bar^{-1} reported for Nafion in the literature [12]. For comparison, the electrical short related current was also determined by cyclic voltammetry from the slope of the CV under N$_2$ atmosphere [13], which yielded a value of $j_0^L = (1.3 \pm 1.25) \times 10^{-3}$ A cm^{-2}. As expected, the observed value was slightly smaller,
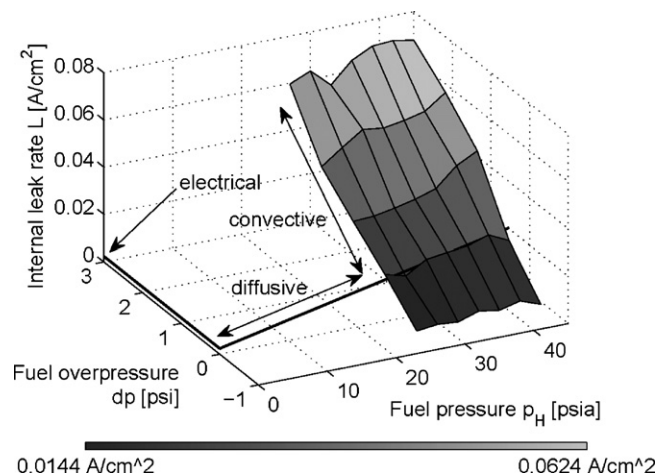
Fig. 9. Result of the deconvolution of leakage current I_L into convective, diffusive (H$_2$) and electrical short components according to Eq. (10) using a small test cell. O$_2$ diffusion was neglected as the oxygen diffusivity through PFSA membranes is typically much smaller than for hydrogen [9].

Table 1
Experimental values for the leakage coefficients and the current density due to electrical shorting determined through a systematic variation of operating pressures. Column 3 provides the equivalent H_2 permeation coefficients (see Ref. [7]).

	Leakage coefficients	Permeation coefficients
Reactant crossover (convective flow)	$L_x = (1.26 \pm 0.08) \times 10^{-2}$ A cm^{-2} psi^{-1}	$(1.9 \pm 0.12) \times 10^{-9}$ mol s^{-1} cm^{-1} bar^{-1}
Reactant crossover (diffusive flow)	$L_H = (6.6 \pm 1.9) \times 10^{-4}$ A cm^{-2} psi^{-1}	$(9.9 \pm 2.8) \times 10^{-11}$ mol s^{-1} cm^{-1} bar^{-1}
Electrical short	$j_0^L = (1.5 \pm 6.3) \times 10^{-3}$ A cm^{-2}	

due to the omission of the O_2-crossover related term, but with a significantly reduced error.

The foregoing discussion demonstrates the power of the operating pressure based leak deconvolution method using polarization fitting. The combination of this method with current mapping as described in the previous sections is straightforward and promises even more detailed insights into membrane and MEA-related degradation phenomena by adding spatial resolution. Although the CV-based determination of electrical shorts appears to deliver greater accuracy (at least for leakage currents in the order of ≈ 1 mA cm^{-2}), this method is not easily performed at the stack level, at least not in minimally invasive fashion. If the voltage ramp is applied to the series combination of all cells, leaky cells will exhibit significantly lower voltages and scan rates, which distorts the voltammograms. On the other hand, operating pressure variation can be performed regardless of leak size and, contrary to cyclic voltammetry, accuracy is expected to improve with leak size.

4. Conclusions

A 10-cell Mk 9 stack was characterized using current/voltage mapping during automotive drive cycle lifetime testing in minimally invasive fashion, i.e. using standard MEA's and plates. At regular intervals polarization scans and localized OCV measurements were performed which were shown to provide useful information about leak formation and location. Using an electrical network model localized leakage current maps can be derived from the OCV profiles, which represent key diagnostic information to monitor MEA- and membrane degradation. The calculations show that reactant transfer leaks cause current reversal at the location of the transfer leak, so that the leakage current maps provide a convenient method of leak location. Further information about the type of leak (convective or diffusive reactant transfer, electrical short) can be gained through a systematic variation of operating conditions.

Acknowledgement

References

[1] J. Stumper, M. Löhr, S. Hamada, J. Power Sources 143 (2005) 150.
[2] J. Stumper, H. Haas, A. Granados, J. Electrochem. Soc. 152 (2005) A837.
[3] S. Srinivasan, E.A. Ticianelli, C.R. Derouin, A. Redondo, J. Power Sources 22 (1988) 359–375.
[4] J. Stumper, R. Rahmani, F. Fuss, Electrochem. Trans. 25 (1) (2009) 1605.
[5] M.K. Debe, A.K. Schmoeckel, G.D. Vernstrom, R. Atanasoski, J. Power Sources 161 (2006) 1002.
[6] R. Borup, et al., Chem. Rev. 107 (2007) 3904.
[7] A.Z. Weber, J. Electrochem. Soc. 155 (6) (2008) B521.
[8] G.–S. Kim, J. St-Pierre, K. Promislow, B. Wetton, J. Power Sources 152 (2005) 210.
[9] M. Inaba, T. Kinumoto, M. Kiriake, R. Umebayashi, A. Tasaka, Z. Ogumi, Electrochim. Acta 51 (2006) 5746.
[10] J. Yu, T. Matsuura, Y. Yoshikawa, Md Nazrul Islam, M. Hori, Electrochem. Solid State Lett. 8 (3) (2005) A156.
[11] E. Moore, Bull. Am. Math. Soc. 26 (1920) 394–395.
[12] A.Z. Weber, J. Newman, J. Electrochem. Soc. 151 (2) (2004) A311.
[13] S.S. Kocha, J.D. Jang, J.S. Yi, AICHE J. 52 (5) (2006) 1916.